Two-Dimensional MXene Modified Electrodes for Improved Anodic Performance in Vanadium Redox Flow Batteries

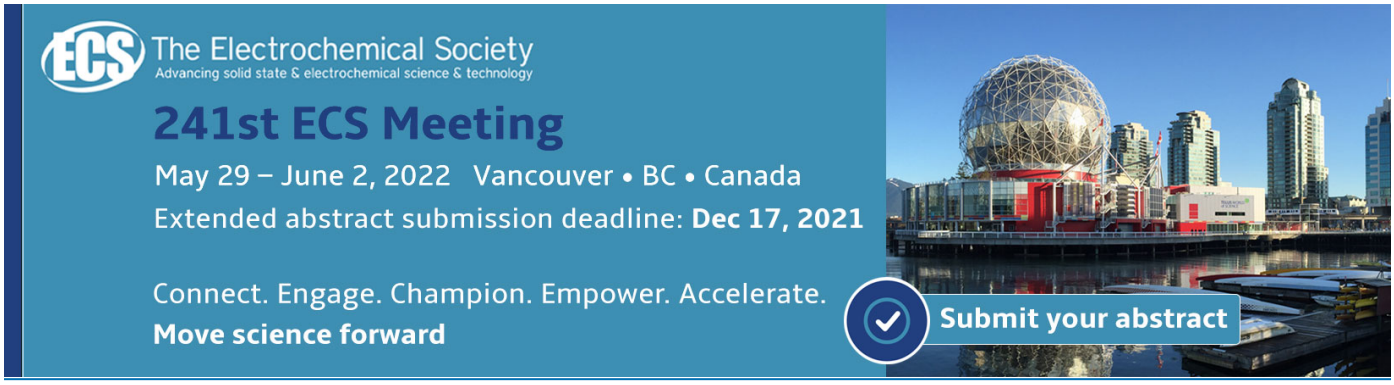

Journal of The Electrochemical Society, 2021 **168** 090518
1945-7111/2021/168(9)/090518/10/$40.00

Two-Dimensional MXene Modified Electrodes for Improved Anodic Performance in Vanadium Redox Flow Batteries

Ali Vala Mizrak,[1] Simge Uzun,[2] Bilen Akuzum,[1,2] Lutfi Agartan,[1] Yury Gogotsi,[2,*] and E. Caglan Kumbur[1,z]

[1]*Electrochemical Energy Systems Laboratory, Department of Mechanical Engineering and Mechanics, Drexel University, Philadelphia, Pennsylvania 19104, United States of America*
[2]*A. J. Drexel Nanomaterials Institute and Department of Materials Science and Engineering, Drexel University, Philadelphia, Pennsylvania 19104, United States of America*

In this work, $Ti_3C_2T_x$ MXene was investigated as electrocatalyst material for the anodic V^{2+}/V^{3+} reaction in vanadium redox flow batteries (VRFBs). A simple drop coating process was established using additive-free, aqueous MXene dispersions to fabricate MXene-coated carbon paper electrodes. The performance of $Ti_3C_2T_x$ as an anodic electrocatalyst was studied using cyclic voltammetry and electrochemical impedance spectroscopy in a three-electrode cell. Furthermore, flow battery testing was performed to determine the performance of the modified electrodes. At a current density of 50 mA cm^{-2}, the electrode with $Ti_3C_2T_x$ loading of 0.2 mg cm^{-2} enabled a 7% higher energy efficiency and 22% higher electrolyte utilization rate than the pristine electrode. At a higher current density (100 mA cm^{-2}), the energy efficiency and electrolyte utilization were increased by 17% and 46%, respectively. At 50% SOC, the coated electrode was able to reach a limiting current density of 220 mA cm^{-2} while maintaining a voltaic efficiency above 80%, whereas the pristine electrode could only reach up to 160 mA cm^{-2} at the same voltaic efficiency. The improved performance was mainly attributed to the enhanced electrode kinetics, increased electrochemically active surface area, and improved wetting properties due to the addition of $Ti_3C_2T_x$ nanoflakes.
 [DOI: 10.1149/1945-7111/ac22cd]

Manuscript submitted July 1, 2021; revised manuscript received August 23, 2021. Published September 9, 2021.

Renewable energy is fast becoming a major sector in the global energy market due to recent technological advances and growing concerns over the environmental impact of fossil fuel emissions. Yet, the renewable energy market is largely constrained by the intermittent nature of solar/wind power production and requires supplementary grid-level energy storage to deliver reliable power under varying loads.[1–3] In that respect, flow batteries are among the most promising and advantageous electrochemical systems available to store energy with capacities ranging from several hundred kWh to multi-MWh. Intrinsically, they offer modular scalability in system design owing to their decoupled energy and power ratings, which enables the flexibility to be able to optimize the volume of the electrolytes and the size of the battery cell separately to meet the specific demands.[4] Among existing flow battery technologies, all-vanadium redox flow batteries (VRFBs) are the most widely studied flow battery chemistries.[5–7]

VRFBs are operated by employing only vanadium and therefore can eliminate the problem of cross-contamination caused by the undesirable transfer of active species through the membrane, causing capacity fade.[8–10] Unlike solid-state systems, the redox reactions take place at active sites across the electrode-electrolyte interface without causing any morphological change and/or phase transformation to the electrodes during charge-discharge cycles. In VRFBs, carbon felt, graphite felt, and carbon paper are the most commonly used electrode materials to date.[11–13] These carbonaceous materials have sufficient electronic conductivity, high porosity, and excellent chemical stability in highly oxidizing environments, which make them ideal candidates for use in VRFBs. However, they intrinsically suffer from the low electrochemically active surface area, insufficient wetting, and poor kinetic reversibility.[14] Therefore, the electrochemical performance can be increased by modifying the surface through two main approaches: in-situ *modification* and *indirect modification.*

In-situ *modification* of the surface of an electrode is categorized by thermal and chemical treatments and other surface treatment techniques (plasma, gamma rays irradiation, etc.) by generating active groups on the electrode surface and also increasing the electrochemically active area by surface roughening, pore formation and crack propagation.[13,15] Alternatively, *indirect modification* implies physical decoration of an electrode surface with nanostructured electrocatalysts or functional materials with high surface area and abundant surface groups.[16] By means of indirect modification, precious metals (e.g., Pt, Ir, Ru, Bi, Au, etc.) have been investigated at first.[12] Besides, studies have also been reported on several metal oxides (e.g., IrO_2, Mn_3O_4, MoO_2, WO_3, PbO_2, and Nb_2O_5), some of which have low cost and are abundant.[17,18] Eventually, the focus has shifted towards carbon-based electrocatalysts such as activated carbon,[19] carbon black,[20] multi-walled and single-walled carbon nanotubes,[21] graphene,[22] reduced graphene oxide,[23] carbon nanowalls,[24] graphene oxide nanoplatelets,[25] nitrogen-doped mesoporous carbon, carbon nanotubes, graphene[26] and carbon spheres[27] to improve the kinetics of the electrode reactions and the overall battery performance. Although various types of nanoparticles have already proven their competence as catalyst materials in VRFBs, a large group of 2D transition metal carbides, nitrides, and carbonitrides referred to as MXenes have not received much attention despite having been first reported a decade ago.[28]

MXenes offer versatile features that distinguish themselves as potential candidates for electrocatalyst applications in RFBs, such as excellent hydrophilicity due to the abundance of surface functional groups, remarkable conductivity (up to 20,000 S cm^{-1}), and electrochemical stability at anodic potentials.[29–33] The general formula of MXenes is $M_{n+1}X_nT_x$, where M stands for a transitional metal, while X represents carbon and/or nitrogen (n = 1–4), and T_x denotes the surface termination groups (–OH, –O, –F), which play a crucial role in energy storage and catalysis applications.[34–39] The most studied MXene to date, titanium carbide ($Ti_3C_2T_x$) is synthesized by selective etching of its MAX phase precursor Ti_3AlC_2.[40,41] $Ti_3C_2T_x$ has found applications in energy storage, electrochemical catalysis, water desalination, electromagnetic interference shielding, optoelectronics, filtration, sensor technologies, etc.[38,42,43] However, very limited research has been published with MXenes in VRFB applications.

To the best of our knowledge, only Wei et al. reported on a preliminary investigation of the catalytic effect of MXenes in VRFBs.[44] As a very first adaptation of MXenes into the flow battery research, Wei et al. employed hollow $Ti_3C_2T_x$ spheres as electrocatalysts to facilitate V^{2+}/V^{3+} redox reactions. They reported that MXene decorated graphite felt anodes achieved an energy efficiency

*Electrochemical Society Fellow.
[z]E-mail: eck32@drexel.edu

of 81.3% at 200 mA cm^{-2} and 75.0% at 300 mA cm^{-2} while maintaining excellent durability during cycling. The increased performance was not only attributed to the increased surface area due to the nanoparticle modification but also the enhanced kinetics. However, the method reported by Wei et al. to modify graphite felts with MXenes necessitates multi-step processing, such as polymer sphere synthesis and thermal treatment. In comparison, homogeneous dispersions and inks of $Ti_3C_2T_x$ for scalable coating processes is an established method;[45] hence, investigating the performance of carbon electrodes coated by additive-free, aqueous MXene dispersions/inks for VRFB applications could offer significant improvements in performance while drastically reducing cost.

In this work, we demonstrate a simple one-step drop coating procedure to modify carbon paper electrodes in VRFBs by using additive-free aqueous colloidal suspensions of delaminated $Ti_3C_2T_x$ MXenes. The electrochemical effect of $Ti_3C_2T_x$ nanoflakes as an anodic electrocatalyst material was investigated for carbon paper electrodes. Aqueous $Ti_3C_2T_x$ dispersion was applied to commercial carbon paper *via* the drop-casting method, which enabled easy and fast modification of the electrodes. To reach specific coating densities, the casting and drying procedure was repeated as many times as required. Respectively, four different coating densities were applied to each electrode, ranging from 0 mg cm^{-2} (no coating) to 0.3 mg cm^{-2}. The concentration range was selected to draw a line between where the effectiveness of the catalytic attribution of $Ti_3C_2T_x$ nanoparticles towards V^{2+}/V^{3+} reactions is maximized and where the mass transport limitations start to hinder the kinetic improvements due to clogging of the porous electrode. Comprehensive electrochemical techniques including cyclic voltammetry (CV), polarization curves, electrochemical impedance spectroscopy (EIS), and charge-discharge cycle analyses have been used. In addition, the electrochemical data was supported with material characterization methods such as X-ray diffraction (XRD) and scanning electron microscopy (SEM) imaging, as well as wetting and electrical conductivity measurements.

Experimental

Electrode preparation.—The $Ti_3C_2T_x$ dispersion was produced following our previous work.[46,47] Before drop-casting, the $Ti_3C_2T_x$ dispersion was probe-sonicated (Fisher Scientific model 505 Sonic Dismembrator, 500 W) in a cooling chamber (−9 °C) for 5 min under a pulse setting of 8 s on and 2 s off and an amplitude of 50%; the probe was fully immersed in the dispersion.

To prepare the MXene modified electrodes, square pieces with a geometric surface area of 10 cm^2 were cut from a commercially available carbon paper (AvCarb 250F). To maintain a homogenous distribution of the nanoparticles across the electrode surface, carbon papers were mildly plasma treated (Harrick Plasma, PDC-32G Plasma Cleaner) in a vacuum chamber (pressure <150 mTorr) for two minutes at medium power setting. For the dispersion, 65 μl of the MXene solution (3.8 mg ml^{-1}) was mixed with 235 μl of DI water that formed 300 μl of MXene suspension in total, containing 0.025 mg of $Ti_3C_2T_x$ particles. This diluted MXene solution of 300 μl was equally applied onto both surfaces of the carbon paper electrodes by a micropipette. Thus, by applying 300 μl of MXene solution with the concentration of 0.083 mg ml^{-1}, a coating density of 0.025 mg cm^{-2} was achieved. Furthermore, upon air-drying on a rack, this procedure was repeated until the intended coating densities of 0.1, 0.2, and 0.3 mg cm^{-2} were acquired for each sample. Accordingly, the MXene modified electrodes were labeled as NC (no coating), MX-1 (0.1 mg cm^{-2}), MX-2 (0.2 mg cm^{-2}), and MX-3 (0.3 mg cm^{-2}), depending on their MXene coating densities.

VRFB cell.—The flow battery operated in this study was a custom-made single cell, which is illustrated as a schematic along with the test station in Fig. 1. The single-cell battery consisted of two graphite current collectors on which interdigitated flow fields were engraved by a CNC machine with a channel depth and width of 1 mm. Three layers of carbon papers were employed at both sides, and the cell was separated with a Nafion 212 (Dupont) membrane, all of which were sandwiched between PVC endplates. To prevent the leakage of the liquid electrolyte and maintain a compression rate of ∼30% on the porous electrodes, single-layer Teflon gaskets with a thickness of 500 microns were employed between the flow fields and the membrane. The cell structure was evenly compressed with six stainless steel screws by applying a torque of 15 in-lbs. The cell was connected to the glass vial tanks containing anolyte and catholyte and to the peristaltic pumps (Cole Palmer) with clear Tygon tubings (Saint-Gobain). During all of the flow tests, the flow rate was maintained at 50 ml min^{-1}.

Electrolyte preparation.—The vanadium electrolyte (1M vanadium − 4M H_2SO_4) was synthesized by mixing vanadium (IV) oxide sulfate hydrate ($VOSO_4 \cdot xH_2O$—97%, Sigma Aldrich) with deionized (DI) water first at about 75 °C and then by slowly adding concentrated sulfuric acid (H_2SO_4–96.3%, Sigma Aldrich) while stirring vigorously. Afterward, the solution was continued to be moderately stirred overnight while maintaining the temperature approximately at 40° C to ensure that the full dissolution of metal salts was achieved. During the flow tests, both anolyte and catholyte volumes employed in the glass vial tanks were adjusted to 20 ml, as such during the precharging stage, the starting volume of the catholyte was 40 ml to maintain the charge balance. Prior to precharging, the electrolytes and the reservoirs were purged with high-purity nitrogen gas (N_2) for 45 min, and a constant N_2 blanket was maintained throughout the flow tests.

Electrochemical characterization.—In order to evaluate the kinetic performance of MXene particles towards the anodic V^{2+}/V^{3+} redox reactions, CV and EIS experiments were performed in the static condition (i.e., no flow) *via* a commercial three-electrode cell setup (Dr. Bob's Cell, Gamry) at room temperature. To utilize as the working electrode in the three-electrode cell, circular-shaped carbon papers with a diameter of 9.53 mm were cut from each electrode sample (NC, MX-1, MX-2, and MX-3) while a silver/silver chloride reference electrode (i.e., Ag/AgCl/3.5 M KCl) was used as the reference electrode, and a graphite rod acted as the counter electrode. 0.5 M vanadium in 2 M sulfuric acid was used as the electrolyte. The measurements were performed with a BioLogic VMP multichannel potentiostat. For CV experiments, the potential window was set between −0.25 V and −0.75 V, and the scan rate was varied from 10 to 50 mV s^{-1}. EIS measurements were potentiostatically controlled with a magnitude of 50 mV between the frequencies of 20 mHz and 100 kHz. All measurements were performed at the open circuit potential (OCP).

Apart from the static CV and EIS experiments, all the flow battery performance measurements were conducted in the dynamic condition with a Scribner Associates 857 redox flow cell test system and the EIS data was collected with the BioLogic VMP multichannel potentiostat. After the precharging, the charge-discharge cycling was conducted at three different current densities (50, 75, and 100 mA cm^{-2}) in order to analyze the battery performance at different operation conditions. The upper voltage limit was maintained at 1.65 V to eliminate possible side reactions as the lower limit was adjusted to 0.8 V. Following the charge-discharge cycling, polarization curves were obtained at a constant 50% state of charge (SOC), which can be assumed as an average charge level of an operating battery. The presumption of the constant SOC at 50% was affirmed by the pre- and post- evaluations of the OCV values. These values were observed to stay within the range of 5 mV. For polarization data, a series of galvanostatic charge and discharge steps with a gradient of 20 mA cm^{-2} was applied for 30 seconds. For every current step, 10 corresponding potential values were recorded as data points until the system reaches its limiting current density. After averaging the collected 10 data points, iR-free voltage values were calculated to diagnose particular overpotentials relating to the kinetic and mass transport properties of the electrodes. After maintaining

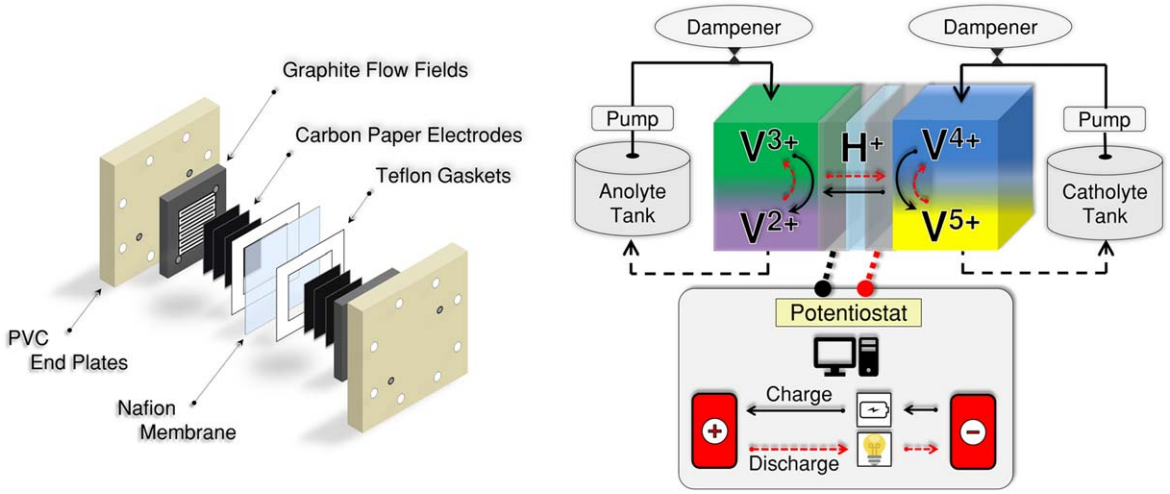

Figure 1. Schematics of the custom-made single cell components, and battery test station.

the polarization curves, EIS measurements were conducted also at 50% SOC. All tests were performed at OCP (≈ 1.43 V) and potentiostatically controlled with a magnitude of 50 mV between the frequencies of 0.5 mHz and 100 kHz. The working electrode was set as the cathode while the reference and counter electrodes were set as the anode in the flow cell.

Material characterization.—The flake size distribution of the prepared MXene solution was measured by dynamic light scattering (DLS, Malvern Instruments, USA). First, a small amount of diluted MXene dispersion was conveyed into a polystyrene cuvette to take five measurements in total from each sample to calculate an average value for the flake size measurements. XRD analysis was performed on a MXene film made *via* vacuum-assisted filtration to reveal its structural properties. The measurement was carried out by a Rigaku Miniflex II–Gen. 6 (Rigaku Co. Ltd. USA) device with Cu K_α (λ = 0.1542 nm) source and graphite K_β filter. The obtained spectra were scanned between 2° to 65° for the 2θ values at 40 kV and with a current of 15 mA.

SEM images were taken on a Zeiss Supra 50 VP microscope with an acceleration voltage of 4 kV to observe and assess how various densities of the MXene coating affect the distribution of the nanoparticles on the porous structure of carbon paper electrodes. The MXene-coated carbon paper electrodes were sputter-coated with Pt/Pd at 40 mA for 40 s (Cressington Scientific 108 Auto, Watford, UK) before imaging. For the wetting angle measurements, circular carbon papers with a diameter of 11 mm were prepared. With a micropipette, 35 μl of DI water was dropped on each sample (NC, MX-1, MX-2, MX-3) and the pictures were taken after 2 minutes.

Finally, a multimeter (Keysight 2400) was used to measure the electrical resistance of the electrodes with a measurement distance of 1 cm. Utilizing a two-point probe along the x-axis and y-axis, eight measurements (sixteen in total), were performed at different locations on the carbon paper electrodes. An average value for the electrical resistance measurements was calculated for each electrode and presented together with the standard deviations.

Results and Discussion

Material and morphological characterization of the electrodes.—The electrode coating procedure began with the processing of the aqueous MXene dispersion, which involved the etching of the precursor MAX phase, Ti_3AlC_2. The XRD results (Fig. 2) revealed a successful etching of the Al layers that are located between the interlayers of $Ti_3C_2T_x$ structures. The (002) peak indicates the expansion and disorder of the interlayer spacing, which was a direct result of the exfoliation of MXene. Moreover, the vanished (014) peak in the XRD of the $Ti_3C_2T_x$ film points out that there was no residual MAX phase in the dispersion. Furthermore, the DLS results indicated that the resulting dispersion obtained after the solution processing mainly consisted of small flakes with an average flake size of 255 nm. Considering the single peak acquired from the DLS measurements, it was concluded that the suspension was consisting of monodispersed MXene nanoflakes.[48]

The hydrophilic MXene nanoparticles greatly improved the wettability of the carbon paper electrodes. The wetting angle for the NC electrode was measured to be ∼98°. Nevertheless, MXene coated electrodes rapidly absorbed all the DI water and presented excellent hydrophilicity (Fig. 3a), which ultimately promoted enhanced surface utilizations.[49,50] In addition, the electrical resistance of the carbon paper electrodes improved slightly after modification with highly conductive $Ti_3C_2T_x$ nanoparticles at all studied coating densities (Fig. 3b).

The morphology of plain and $Ti_3C_2T_x$ decorated carbon papers is shown in Fig. 4. Compared to the MXene-coated electrodes, the individual carbon fibers of the pristine electrode (NC) and their fabricated cross-linked structure can be visually identified in Figs. 4a–4b. In addition, these fibers have binder material that holds them together. In all of the SEM images, a very dense binder distribution over the entire surface of the carbon papers was quite noticeable, which may have led to the increased mass transport limitations as a result of excessive particle loading and/or accumulation.[20] Even though the binder could be intensely identified on the structure of the NC electrode, the surface of the individual fibers was found to be generally much smoother and easy to observe compared to the MXene coated electrodes.

As the coating density of MXene was gradually increased from 0 mg cm^{-2} (NC) to 0.3 mg cm^{-2} (MX-3), the surface roughening of the carbon fibers became much more distinguishable. This change was caused by the aggregation and accumulation of $Ti_3C_2T_x$ particles all over the surface of the fiber/binder composite structure. In Figs. 4e–4f, a more optimal particle distribution on the carbon fibers of the electrode MX-2 could be observed. In particular, the MXene nanoparticles on this electrode seemed to be evenly dispersed (i.e., similar to those of the NC and MX-1 electrodes), and no apparent clogging was present. Since the conventional porous and fibrous structure of carbon papers was still readily observable, it is expected that the coating density of 0.2 mg cm^{-2} did not cause any over-accumulation of MXene nanoparticles. In fact, the uniform dispersion of nanoparticles throughout the porous electrode network may enhance the electrochemically active surface area without causing any serious mass transport limitations, while increasing the electrical conductivity. Yet, the uniformity of distribution of the $Ti_3C_2T_x$ nanoparticles appears to decrease with further increase in MXene loading, as seen on the MX-3 electrode (Figs. 4g–4h). This

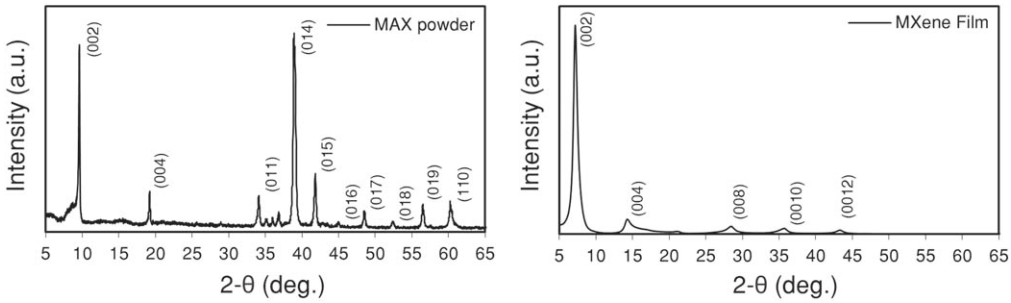

Figure 2. XRD results; for MAX powder (left), and MXene film (right).

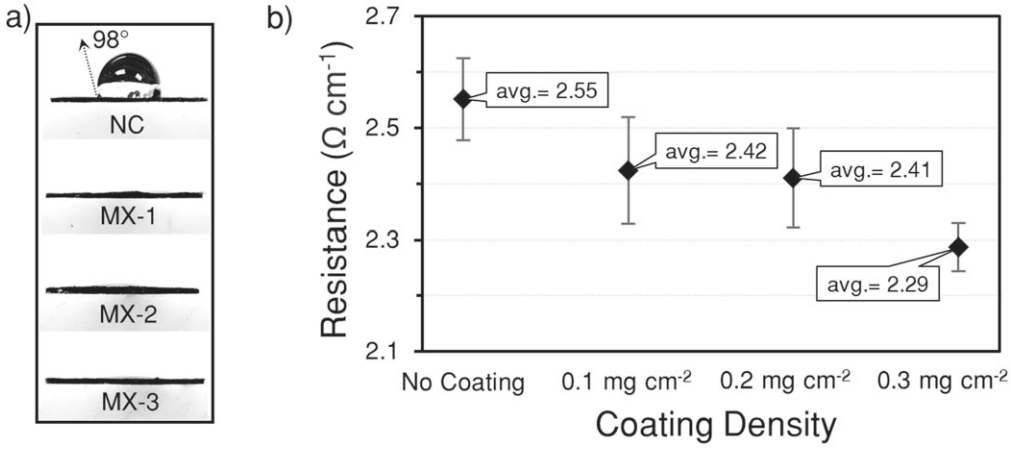

Figure 3. (a) Wetting behavior of different electrodes, and; (b) resistance values of the electrodes (standard deviations: SD_{NC}: 0.146; $SD_{MX\text{-}1}$: 0.192; $SD_{MX\text{-}2}$: 0.178; $SD_{MX\text{-}3}$: 0.085).

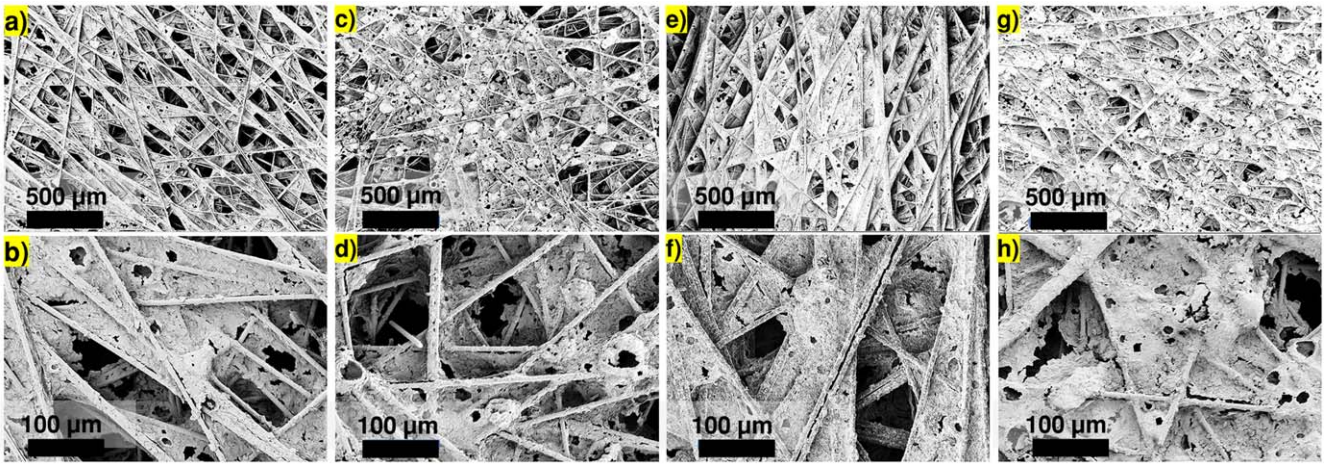

Figure 4. SEM images of the electrodes (a)–(b) NC; (c)–(d) MX-1; (e)–(f) MX-2; (g)–(h) MX-3 in two magnifications of 50x and 250x, respectively.

can be explained by stacking and aggregation of excess amount of $Ti_3C_2T_x$ flakes. For this reason, the coating density of 0.3 mg cm^{-2} was chosen as the highest $Ti_3C_2T_x$ loading studied in this work.

Following every successive coating procedure, $Ti_3C_2T_x$ flakes were observed to establish alternative/varying networks between the carbon fibers. These new structural formations are expected to enhance the surface area of the electrode by creating ample reaction sites for the active ions; however, they may also result in the blockage of the channels within the porous structure that are essential for liquid electrolyte penetration/circulation through the carbon paper electrodes.[51–53] Moreover, besides the alteration of the porous structure, excessive accumulation of $Ti_3C_2T_x$ flakes could cause individual carbon fibers to become buried under the overabundant nanoparticles. This would substantially transform the intrinsic morphology of porous carbon paper electrodes, resulting in a critical reduction of the electrochemically active surface area. Both of these occurrences would increase mass transport overpotentials, as explained in this study.

Electrochemical performance.— *Cyclic voltammetry.*—CV measurements were performed to identify the catalytic effect of $Ti_3C_2T_x$ flakes towards the anodic V^{2+}/V^{3+} redox couple. As seen in Fig. 5a, the anodic/cathodic peaks induced by the anode reactions showed major differences, implying significant changes between the catalytic activity of different electrodes. Within the potential range of the CV measurement positioned between −0.75 and −0.25 V (vs Ag/

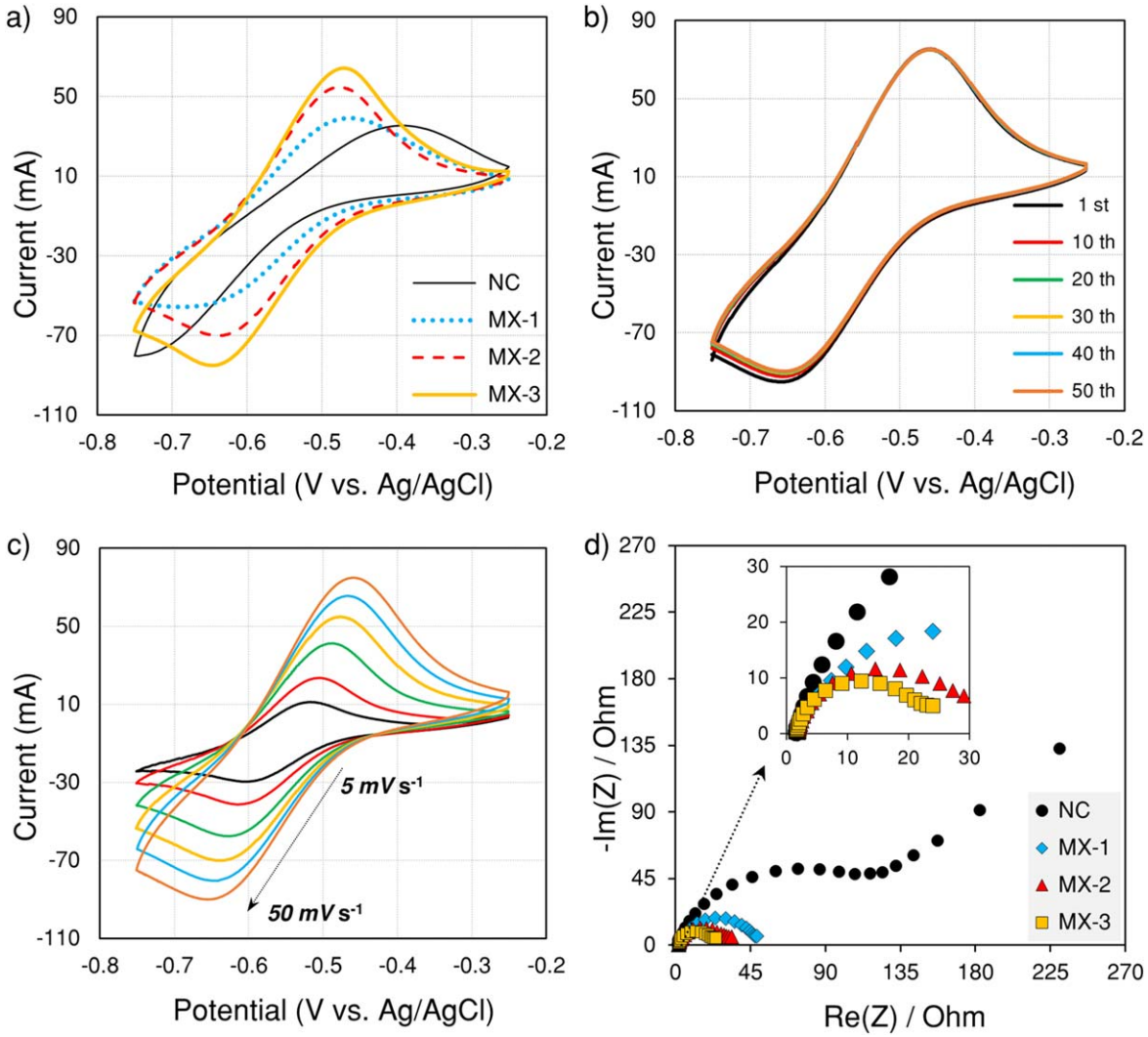

Figure 5. CVs recorded between the potentials of −0.75 V and −0.25 V in respect to Ag/AgCl reference electrode (a) with all the electrodes at a scan rate of 30 mV s^{-1} for comparing the performances; (b) with the MX-2 electrode as a sweeping scan for 50 times at a scan rate of 50 mV s^{-1}; (c) with the MX-2 electrode at several scan rates ranging from 5 mV s^{-1} to 50 mV s^{-1}. (d) Nyquist plots of the NC, MX-1, MX-2 and MX-3 electrodes were obtained with a three-electrode cell setup at OCP between the frequencies of 20 mHz and 100 kHz with an amplitude of 50 mV.

AgCl), the redox peaks of the pristine electrode exhibited relatively poor performance as compared to $Ti_3C_2T_x$ decorated electrodes, which indicates that the catalytic activity of the pristine carbon paper electrode is intrinsically limited towards the V^{2+}/V^{3+} redox couple. Moreover, $Ti_3C_2T_x$ decorated electrodes provided more reversible CV curves due to the increased electrochemical activity. The reversibility of this system can be quantitatively determined by the peak separation values (ΔE_p) and the ratio of peak currents (I_{pa}/I_{pc}). With $Ti_3C_2T_x$ modifications, the tested electrodes produced more prominent anodic and cathodic peaks that lowered the ΔE_p values, which were obtained as 343, 206, 154, and 173 mV for NC, MX-1, MX-2, and MX-3 electrodes, respectively (Fig. 5a).

Besides the catalytic activity of $Ti_3C_2T_x$ particles towards the V^{2+}/V^{3+} redox couple, the durability of the coating was also investigated by running 50 repetitive CV scans with the MX-2 electrode at 50 mV s^{-1} (Fig. 5b). Within the acquired potential window, overlapping curves were maintained without any significant decay at their peak current levels, which is a strong indication of the endurance and the stability of the $Ti_3C_2T_x$ particles as an electrocatalyst material at negative potentials.

In addition to significant improvements in ΔE_p values that relate to improved voltaic efficiency due to decreased overpotentials, the ratio of anodic and cathodic peak currents (I_{pa}/I_{pc}) was approximated to 1.0, which is also an indicator for better reversibility.[54] Based on the corresponding data derived from the CV curves for the MX-2 electrode shown in Fig. 5c, the ΔE_p value was found to be 75 mV at the scan rate of 5 mV s^{-1} and I_{pa}/I_{pc} was calculated as 1.04. Therefore, the reversibility, which is a direct measure of the kinetics of the VRFB electrode reactions, was significantly better on the electrodes modified with $Ti_3C_2T_x$ nanoparticles, which aligns with the performances achieved by the MX-2 and MX-3 electrodes.

Figure 5c shows the CV curves of the MX-2 electrode at different scan rates. The relationship between the anodic/cathodic peak currents and the square root of scan rates exhibited a linear characteristic with the R^2 values calculated as 0.*9954* and 0.9975 for the anodic and cathodic reactions, respectively. The linearity between these parameters implies that the limiting step of the V^{2+}/V^{3+} redox reaction was diffusion, which takes place between electrode-electrolyte interface.[55] Moreover, the numerical analysis was performed to quantify the diffusion coefficients of the anodic V^{2+}/V^{3+} redox reactions, and then the reaction rate constants were obtained for the system.[54] The diffusion coefficients for V^{+2} and V^{+3} ions were calculated as $D_{(VII)} = 2.24 \times 10^{-5}$ $cm^2.s^{-1}$, $D_{(VIII)} = 2.44 \times 10^{-5}$ $cm^2.s^{-1}$ while the reaction rate constants were found as $k_{(VII)} = 1.27 \times 10^{-3}$ $cm.s^{-1}$, and $k_{(VIII)} = 2.02 \times 10^{-3}$ $cm.s^{-1}$, respectively. To further investigate the electrocatalytic activity of

$Ti_3C_2T_x$ particles, EIS measurements were carried out with the same setup at OCV (Fig. 5d). The semicircle-shaped loop of a Nyquist plot constituted at the high-frequency region would reflect the charge transfer process of an electrode reaction. In other words, the radius of a semicircle at the high-frequency region in a Nyquist plot refers to the degree of charge transfer resistance. In line with the reported CV results, EIS data also pointed out that the charge transfer resistance of the V^{2+}/V^{3+} redox reaction was remarkably decreased with the increased MXene loading, which also demonstrates the enhanced catalytic activity of $Ti_3C_2T_x$ nanoparticles towards anode reactions of the V^{2+}/V^{3+} redox couple.

Polarization curves.—The polarization curves were obtained to assess the flow battery performance of MXene-coated carbon paper electrodes and to investigate the voltage range of the VRFB with respect to applied and/or utilized current densities at the preferred flow rate.

The polarization curves for pristine and MXene-coated electrodes are shown in Fig. 6. In a polarization curve, the activation losses related to electrode kinetics would be largely dominating at lower current densities whereas the mass transport overpotentials are expected to dominate at higher current densities.[56] The results showed that the electrodes modified with MXene flakes exhibited the best performances at all current density regions compared to the pristine carbon paper electrode. Accordingly, the improved electrode kinetics resulted in much lower activation overpotentials for all the MXene-coated electrodes, which improved the voltaic efficiencies of the cells over a broad range of current densities (up to 160 mA cm^{-2}).

It is also important to note that increasing the current density above 160 mA cm^{-2} seems to result in mass transport limitations at different levels for the coated electrodes. While the MX-2 electrode was able to maintain a prominent voltaic efficiency over a wide range of the current densities (0–220 mA cm^{-2}) without showing any notable decline in its performance, the MX-1 and MX-3 electrodes were able to operate only up to 160 mA cm^{-2} and 180 mA cm^{-2}, respectively. In addition, even though the NC electrode reached a higher limiting current density value of 200 mA cm^{-2} as compared to MX-1 and MX-3, the higher activation overpotential appeared to cause the NC electrode to operate at much lower voltaic efficiencies, and hence its voltaic efficiency had dropped under 80% when the current density was above 160 mA cm^{-2}. Among the tested electrodes, the MX-2 electrode was found to exhibit the best electrochemical performance due to its lower activation overpotentials and optimal mass transport. As a result, the MX-2 electrode was able to perform over a broader range of current density (up to 220 mA cm^{-2}) with higher voltaic efficiencies as compared to other electrodes.

When the performance of the MX-3 electrode is analyzed, it appears that the MXene coating density of 0.3 mg cm^{-2} started to hinder the performance of the electrode, especially above 100 mA cm^{-2}. This can be attributed to the mass transport limitations arising from the clogging effect of the excess amount of $Ti_3C_2T_x$ flakes. However, the MX-3 electrode still performed better when compared to the MX-1 electrode, indicating that the favorable effect of the MXene coating on activation overpotential dominates the increased mass transport limitations. This result was also consistent with the SEM images (Fig. 4), which pointed out that the MXene loading density of more than 0.2 mg cm^{-2} resulted in a higher accumulation of the $Ti_3C_2T_x$ flakes, eventually increasing the penetrability resistance of the electrolyte by clogging the pores. Basically, in parallel with the CV results, polarization curve analysis indicated that the addition of $Ti_3C_2T_x$ flakes enhances the overall electrode performance by improving the catalytic activity and providing more active sites for the V^{2+}/V^{3+} redox reactions.

EIS analysis.—In addition to the polarization curves, EIS measurements were conducted to acquire qualitative data regarding the electrode kinetics as well as the mass transport characteristics of the electrodes. Similar to the EIS result presented in Fig. 5d, at the high-frequency region of the Nyquist plots, there are only ohmic and charge transfer resistances. While the ohmic resistance addresses the electronic and ionic losses, the latter distinguishes the kinetic performance of the electrodes. Similarly, mass transport characteristics of a VRFB can be analyzed at the low-frequency region of a Nyquist plot. However, due to the nature of the EIS method, special modifications to the testing setup are required in order to collect data at the low-frequency region in a dynamic system. To eliminate the fluctuations caused by the peristaltic pump pulses, dampeners or gravity siphons must be utilized. These fluctuations within the liquid electrolyte could induce disturbances at low frequencies by physically altering the diffusion layer, which leads to distortions in data collection.[57] In this study, for useful data acquisition at lower frequencies, pulse dampeners were utilized to stabilize the

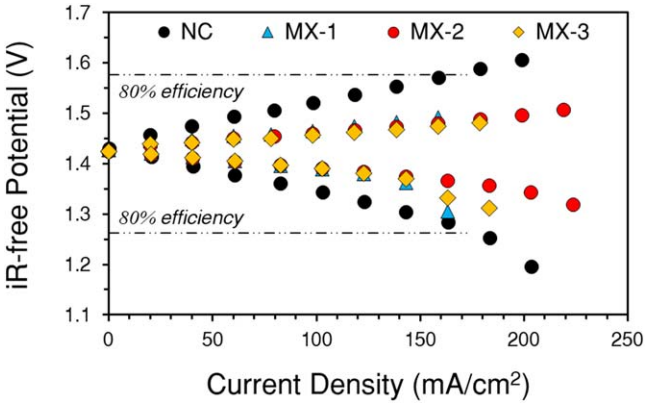

Figure 6. Polarization curves of the NC, MX-1, MX-2 and MX-3 electrodes were obtained at 50% SOC at a flow rate of 50 ml min^{-1}.

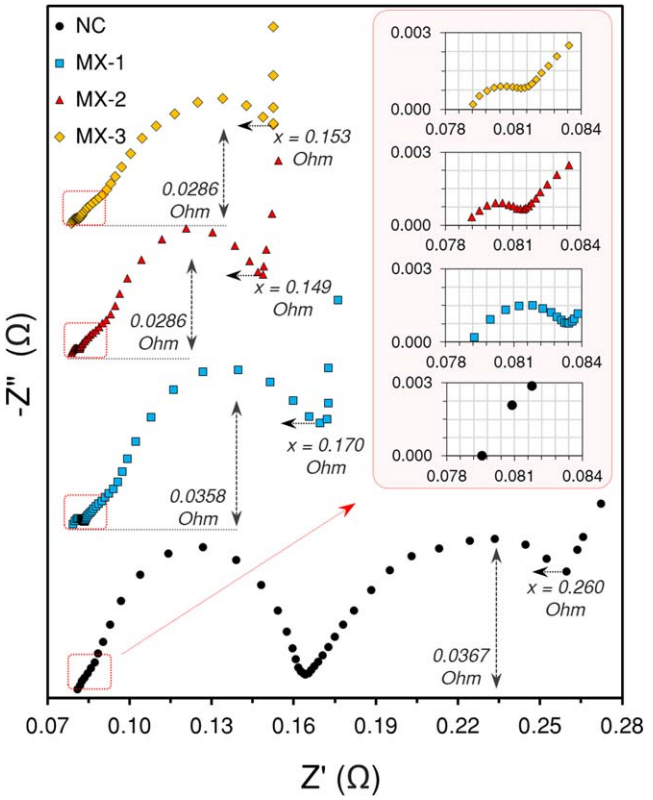

Figure 7. Nyquist plots of the NC, MX-1, MX-2, and MX-3 electrodes were obtained in the dynamic condition with a flow rate of 50 ml min^{-1} (*Both axes were offset*).

electrolyte flow, and the Nyquist plots were successfully collected at the OCP as the SOC was maintained at 50%. As indicated in Fig. 7, the EIS results are presented as offset values. The resistance values on the x-axis were offset due to the misleading deviations caused by test setup connections whereas the y-axis was offset with regard to the ease of comparison.

The analysis of the semi-circles at the high-frequency region in the Nyquist plots indicates that the charge transfer resistance of the electrodes decreased drastically with the modification of MXene flakes. Initially, for the MX-1 electrode, the radius of the first semi-circle decreased from about 0.04 ohm (NC) to about 0.003 ohms. Furthermore, with the increasing amount of $Ti_3C_2T_x$, the radius of the same semi-circle decreased more to about 0.0015 ohms for the MX-2 and MX-3 electrodes, which is a value approximately 26 times smaller than 0.04 ohm (NC). Thus, the equivalent values of 0.0015 ohms for the MX-2 and MX-3 electrodes at the high-frequency region showed that these electrodes would behave similarly at low current densities, where the activation polarization is the dominant factor. This assumption was confirmed by the polarization curves (Fig. 6).

Furthermore, the second semi-circles related to mass transport properties show that the cell with the MX-2 electrodes exhibited the most favorable mass transport characteristics due to the smallest radius of its second semi-circle. The EIS data also suggest that although the MX-2 and MX-3 electrodes had similar kinetic performances, the MX-2 electrode outperformed the MX-3 electrode, which indicated a higher mass transport limitation due to the greater radius (0.031 ohm) of its low-frequency semi-circle. This value was found as 0.029 ohms for the MX-2 electrode, suggesting that among the tested electrodes, the optimal coating distribution seems to be achieved with the MXene coating density of 0.2 mg cm^{-2}.

Charge/discharge cycling.—To further analyze the trade-off between the improved activation kinetics and the restrained mass transport behavior caused by $Ti_3C_2T_x$ coating of the carbon paper electrodes, a series of charge-discharge cycling tests at various current densities (50, 75, and 100 mA cm^{-2}) were conducted at a constant flow rate of 50 ml min^{-1}, and the results are shown in Fig. 8. In addition to understanding the intrinsic synergy between the kinetics and the mass transport characteristics, overall system energy efficiencies at different current densities were calculated by analyzing the voltaic and coulombic efficiencies. Similarly, the electrolyte utilization rates (i.e., depth of discharge (DoD)) were calculated for all the electrodes. If a VRFB can reach a higher DoD, the system cost of the battery can be effectively curtailed by decreasing the necessary amount of the expensive vanadium electrolyte for the same level of energy capacity.[58–60]

As seen in Figs. 8a–8c, the performance of the NC electrode declined immensely with the increased current density, which indicates that the kinetic properties of the pristine NC electrode restrict its usage to only lower current densities. Accordingly, the pristine electrodes exhibited the lowest electrolyte utilization rates at all current densities along with the lowest efficiency values (Table I). The energy efficiencies of the NC electrode were found to be 85%, 75%, and 66% at the current densities of 50, 75, and 100 mA cm^{-2}, respectively. Nonetheless, the electrodes modified with MXene flakes outperformed the pristine NC electrode at all current densities. In correlation with the polarization curves, MXene-modified electrodes were observed to perform very similarly in terms of the discharge voltages over a significant period of time until the mass transport capabilities of each electrode have become the performance determining factor. When the mass transport overpotentials started to dominate due to the reduced concentration of active ions within the anolyte, the performance of the MX-1 and MX-3 electrodes started to decline,[61] while the MX-2 electrode maintained the linearity on the curve due to better mass transport characteristics.

At the initial linear parts of the discharge curves, where the kinetic losses are dominating, discharge voltages of the MX-1 electrode were recorded about 0.01 V lower compared to the MX-2 and MX-3 electrodes. At that region, the discharge curves of the MX-2 and MX-3 electrodes mostly overlapped, showing almost identical kinetic activations. With the increasing current densities, the electrolyte utilization rates started to drop, as expected, for all tested electrodes due to the increased activation and the mass transport overpotentials. The efficiencies for the coated electrodes showed minor deviations, but they were higher than the efficiencies of the pristine electrode (Table I). When the MXene-coated electrodes are compared, an appreciable amount of differences in electrolyte utilization rates was only observed. This was basically because of the alteration in mass transport capabilities, which was caused by the varying distribution characteristic of the $Ti_3C_2T_x$ flakes depending on the coating densities.

With regards to the mass transport capabilities of the MXene-coated electrodes, the MX-1 electrode exhibited the lowest DoD among the modified electrodes due to its limited mass transport behavior, which is on par with the polarization curves analysis. The DoDs for all the electrodes were presented as a bar graph in Fig. 8d. Within the potential window ranging from 0.8 V to 1.65 V, the cell with the MX-2 electrode was able to use 88% of the theoretical capacity while operating at the current density of 50 mA cm^{-2}, which was the highest capacity utilization achieved in this study (Fig. 8a). Under the same conditions, the cells with NC, MX-1, and MX-3 electrodes exhibited discharge rates of 66%, 71%, and 80%, respectively.

The enhanced performance observed for the MX-2 electrode can be attributed to the established balance between the enhanced kinetic performance (i.e., catalytic effect of MXene particles towards the V^{2+}/V^{3+} redox couple) and better mass transport capabilities of the carbon paper electrodes with the optimal coating density of 0.2 mg cm^{-2}. This optimal balance resulted in outstanding DoD levels and enabled higher SOC rates while charging, which ultimately yielded enhanced electrolyte utilization higher efficiencies.

Our findings demonstrated that the MXene modification of carbon paper electrodes resulted in significantly enhanced electrochemical performance in VRFBs. The $Ti_3C_2T_x$ flakes increased the electrical conductivity and improved the wetting properties of pristine carbon paper electrodes, which enabled better kinetic activation and mass transport properties. In particular, the abundant surface termination groups on the surface of MXene nanoparticles appeared to play a key role in increasing the electrochemically active surface area by enhancing wetting properties and facilitating the anode reactions of the $V^{2+/}V^{3+}$ redox couple.[62–67] Besides the active surface groups, delaminated $Ti_3C_2T_x$ flakes with an average particle size of 255 nm created newly formed and abundant physical surfaces throughout the porous electrode, which also contributed to lower activation overpotentials. However, it is important to note that there is a limit for enhancing the performance of the carbon paper electrodes due to their inherent structural constraints. Excessive amounts of MXene nanoparticles on carbon paper electrodes may hinder the battery performance by blocking electrolyte penetration through the porous structure.

Conclusions

We have demonstrated that $Ti_3C_2T_x$ MXene modification of carbon paper electrodes improves the electrochemical performance of VRFBs. A simple, scalable, and binder-free drop-casting process, free from long and energy-consuming thermal and chemical post-treatments, has been introduced. MXene-coated carbon paper electrodes exhibited remarkably increased electrocatalytic activity towards V^{2+}/V^{3+} redox reactions by decreasing the activation overpotential. The SEM images have shown that an optimal distribution of $Ti_3C_2T_x$ flakes was attained at 0.2 mg cm^{-2}. This optimal loading density was found to maximize the electrochemically active surface area by creating active sites and improving the wetting of the hydrophobic carbon paper. For the MX-2 electrode, due to these improvements, the activation overpotentials were

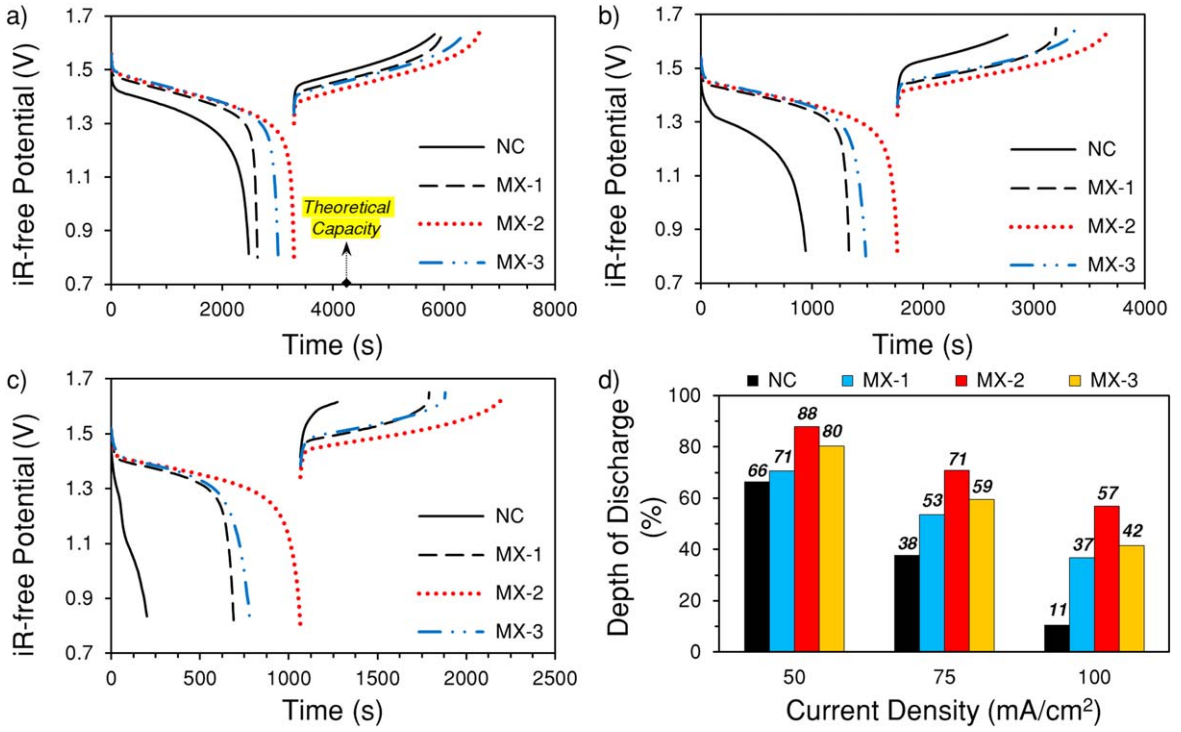

Figure 8. Charge-discharge cycle curves for all the electrodes with the flow rate of 50 ml min^{-1} at (a) 50 mA cm^{-2}; (b) 75 mA cm^{-2}; (c) 100 mA cm^{-2}; (d) the bar graph comparison of the calculated depth of discharge percentages for all the electrodes in respect to the employed current density values of 50, 75 and 100 mA cm^{-2}.

Table I. Efficiencies, specific discharge capacities, and depth of discharge values of the VRFB cells with NC, MX-1, MX-2, and MX-3 anodes.

Electrode	Current Density (mA cm^{-2})	ηV (%)	ηC (%)	ηE (%)	SDC (Ah l^{-1})	DoD (%)
NC	50	86	98	85	17	66
	75	78	95	75	10	38
	100	70	95	66	3	11
MX-1	50	93	99	92	18	71
	75	90	94	85	14	53
	100	87	95	83	10	37
MX-2	50	93	99	92	23	88
	75	90	94	85	18	71
	100	88	94	83	15	57
MX-3	50	93	99	92	21	80
	75	90	93	83	15	59
	100	86	96	82	11	42

dropped and no significant aggravation of the mass transport limitations was observed. According to the polarization curves, the limiting current density of 220 mA cm^{-2} was achieved at 50% SOC with a voltaic efficiency higher than 80% for the MX-2 electrode. Furthermore, the charge-discharge cycling tests also showed that the MX-2 electrode had the best battery performance at all studied current densities with much higher DoD rates. At a current density of 50 mA cm^{-2}, the MX-2 electrode had an energy efficiency of 92% with an electrolyte utilization rate of 88%. When the current density was increased to 100 mA cm^{-2}, these values were maintained as 83% and 57%, respectively, which were 17% and 46% higher than the energy efficiency and electrolyte utilization rates of the pristine NC electrode. Finally, it is noteworthy that although the MXene showed a significant catalytic effect towards the anodic V^{2+}/V^{3+} redox couple, mass transport capabilities of the electrodes in such electrochemical systems should be fully considered since this type of porous electrodes are inherently susceptible to clogging due to excessive coating densities.

Acknowledgments

The authors would like to thank the National Science Foundation (Grant # 2034108) for supporting this work. Development of MXenes for electrochemical applications by S.U. and Y.G. was supported by the Fluid Interface Reactions, Structures, and Transport (FIRST) Center, an Energy Frontier Research Center (EFRC) funded by the U.S. Department of Energy, Office of Science, Office of Basic Energy Sciences. The authors acknowledge the Materials Characterization Core (MCC) facility at Drexel University for providing access to characterization tools. The authors would also like to acknowledge AvCarb Material Solutions for supplying the electrode materials.

Data availability statement

N.A

ORCID

Ali Vala Mizrak https://orcid.org/0000-0002-0811-2512
Simge Uzun https://orcid.org/0000-0002-0469-1772
Bilen Akuzum https://orcid.org/0000-0002-8555-0022
Lutfi Agartan https://orcid.org/0000-0002-5850-4661
Yury Gogotsi https://orcid.org/0000-0001-9423-4032
E. Caglan Kumbur https://orcid.org/0000-0002-2363-7560

References

1. M. Skyllas-Kazacos, C. Menictas, and T. Lim, "Redox flow batteries for medium-to large-scale energy storage." *Electricity Transmission, Distribution and Storage Systems* (Woodhead Publishing, United Kingdom)Ch 12, 398 (2013).
2. G. Papaefthymiou and K. Dragoon, "Towards 100% renewable energy systems: uncapping power system flexibility." *Energy Policy*, **92**, 69 (2016).
3. T. M. Gür, "Review of electrical energy storage technologies, materials and systems: challenges and prospects for large-scale grid storage." *Energy Environ. Sci.*, **11**, 2696 (2018).
4. L. F. Arenas, C. Ponce de León, and F. C. Walsh, "Engineering aspects of the design, construction and performance of modular redox flow batteries for energy storage." *Journal of Energy Storage*, **11**, 119 (2017).
5. T. Jirabovornwisut, S. Kheawhom, Y.-S. Chen, and A. Arpornwichanop, "Optimal operational strategy for a vanadium redox flow battery." *Comput. Chem. Eng.*, **136**, 106805 (2020).
6. P. Alotto, M. Guarnieri, and F. Moro, "Redox flow batteries for the storage of renewable energy: a review." *Renew. Sustain. Energy Rev.*, **29**, 325 (2014).
7. M. Skyllas-Kazacos, "New all-vanadium redox flow cell." *J. Electrochem. Soc.*, **133**, 1057 (1986).
8. K. Lourenssen, J. Williams, F. Ahmadpour, R. Clemmer, and S. Tasnim, "Vanadium redox flow batteries: a comprehensive review." *Journal of Energy Storage*, **25**, 100844 (2019).
9. K. W. Knehr and E. C. Kumbur, "Role of convection and related effects on species crossover and capacity loss in vanadium redox flow batteries." *Electrochem. Commun.*, **23**, 76 (2012).
10. P. A. Boettcher, E. Agar, C. R. Dennison, and E. C. Kumbur, "Modeling of ion crossover in vanadium redox flow batteries: a computationally-efficient lumped parameter approach for extended cycling." *J. Electrochem. Soc.*, **163**, A5244 (2015).
11. S. Zhong, C. Padeste, M. Kazacos, and M. Skyllas-Kazacos, "Comparison of the physical, chemical and electrochemical properties of rayon- and polyacrylonitrile-based graphite felt electrodes." *J. Power Sources*, **45**, 29 (1993).
12. B. Sun and M. Skyllas-Kazakos, "Chemical modification and electrochemical behavior of graphite fibre in acidic vanadium solution." *Electrochim. Acta*, **36**, 513 (1991).
13. H. Zhang, X. Li, and J. Zhang, *Redox Flow Batteries: Fundamentals and Applications.* (CRC Press, Boca Raton, FL) (2017)9781498753944.
14. E. Agar, C. R. Dennison, K. W. Knehr, and E. C. Kumbur, "Identification of performance limiting electrode using asymmetric cell configuration in vanadium redox flow batteries." *J. Power Sources*, **225**, 89 (2013).
15. M. Gencten and Y. Sahin, "A critical review on progress of the electrode materials of vanadium redox flow battery." *Int. J. Energy Res.*, **44**, 7903 (2020).
16. L. Wei, T. S. Zhao, L. Zeng, Y. K. Zeng, and H. R. Jiang, "Highly catalytic and stabilized titanium nitride nanowire array-decorated graphite felt electrodes for all vanadium redox flow batteries." *J. Power Sources*, **341**, 318 (2017).
17. M. Rychcik and M. Skyllas-Kazacos, "Evaluation of electrode materials for vanadium redox cell." *J. Power Sources*, **19**, 45 (1987).
18. K. J. Kim, M. S. Park, J. H. Kim, U. Hwang, N. J. Lee, G. Jeong, and Y. J. Kim, "Novel catalytic effects of Mn_3O_4 for all vanadium redox flow batteries.." *Chem Commun (Camb)*, **48**, 5455 (2012).
19. G. J. W. Radford, J. Cox, R. G. A. Wills, and F. C. Walsh, "Electrochemical characterization of activated carbon particles used in redox flow battery electrodes." *J. Power Sources*, **185**, 1499 (2008).
20. D. Aaron, S. Yeom, K. D. Kihm, Y. Ashraf Gandomi, T. Ertugrul, and M. M. Mench, "Kinetic enhancement via passive deposition of carbon-based nanomaterials in vanadium redox flow batteries." *J. Power Sources*, **366**, 241 (2017).
21. W. Li, J. Liu, and C. Yan, "Modified multiwalled carbon nanotubes as an electrode reaction catalyst for an all vanadium redox flow battery." *J. Solid State Electrochem.*, **17**, 1369 (2013).
22. G. Hu, M. Jing, D.-W. Wang, Z. Sun, C. Xu, W. Ren, H.-M. Cheng, C. Yan, X. Fan, and F. Li, "A gradient bi-functional graphene-based modified electrode for vanadium redox flow batteries." *Energy Storage Mater.*, **13**, 66 (2018).
23. M. H. Moghim, R. Eqra, M. Babaiee, M. Zarei-Jelyani, and M. M. Loghavi, "Role of reduced graphene oxide as nano-electrocatalyst in carbon felt electrode of vanadium redox flow battery." *J. Electroanal. Chem.*, **789**, 67 (2017).
24. Z. González, S. Vizireanu, G. Dinescu, C. Blanco, and R. Santamaría, "Carbon nanowalls thin films as nanostructured electrode materials in vanadium redox flow batteries." *Nano Energy*, **1**, 833 (2012).
25. P. Han, H. Wang, Z. Liu, X. Chen, W. Ma, J. Yao, Y. Zhu, and G. Cui, "Graphene oxide nanoplatelets as excellent electrochemical active materials for VO^{2+}/VO_2^+ and V^{2+}/V^{3+} redox couples for a vanadium redox flow battery.." *Carbon*, **49**, 693 (2011).
26. J. Jin, X. Fu, Q. Liu, Y. Liu, Z. Wei, K. Niu, and J. Zhang, "Identifying the active site in nitrogen-doped graphene for the VO^{2+}/VO_2^+ redox reaction.." *ACS Nano*, **7**, 4764 (2013).
27. Y. Zhao, L. Yu, X. Qiu, and J. Xi, "Carbon layer-confined sphere/fiber hierarchical electrodes for efficient and durable vanadium flow batteries." *J. Power Sources*, **402**, 453 (2018).
28. M. Naguib, M. Kurtoglu, V. Presser, J. Lu, J. Niu, M. Heon, L. Hultman, Y. Gogotsi, and M. W. Barsoum, "Two-dimensional nanocrystals produced by exfoliation of Ti_3AlC_2." *Adv. Mater.*, **23**, 4248 (2011).
29. C. J. Zhang, B. Anasori, A. Seral-Ascaso, S. H. Park, N. McEvoy, A. Shmeliov, G. S. Duesberg, J. N. Coleman, Y. Gogotsi, and V. Nicolosi, "Transparent, flexible, and conductive 2D Titanium Carbide (MXene) films with high volumetric capacitance." *Adv. Mater.*, **29**, 1702678 (2017).
30. A. D. Dillon, M. J. Ghidiu, A. L. Krick, J. Griggs, S. J. May, Y. Gogotsi, M. W. Barsoum, and A. T. Fafarman, "Highly conductive optical quality solution-processed films of 2D titanium carbide." *Adv. Funct. Mater.*, **26**, 4162 (2016).
31. B. Anasori, M. R. Lukatskaya, and Y. Gogotsi, "2D metal carbides and nitrides (MXenes) for energy storage." *Nature Reviews Materials*, **2**, 16098 (2017).
32. X. Sang, Y. Xie, M. W. Lin, M. Alhabeb, K. L. Van Aken, Y. Gogotsi, P. R. C. Kent, K. Xiao, and R. R. Unocic, "Atomic defects in monolayer titanium carbide ($Ti_3C_2T_x$) MXene.." *ACS Nano*, **10**, 9193 (2016).
33. T. S. Mathis, K. Maleski, A. Goad, A. Sarycheva, M. Anayee, A. C. Foucher, K. Hantanasirisakul, C. E. Shuck, E. A. Stach, and Y. Gogotsi, "Modified MAX Phase synthesis for environmentally stable and highly conductive Ti3C2 MXene." *ACS Nano*, **15**, 6420 (2020).
34. S. Uzun, S. Seyedin, A. L. Stoltzfus, A. S. Levitt, M. Alhabeb, M. Anayee, C. J. Strobel, J. M. Razal, G. Dion, and Y. Gogotsi, "Knittable and washable multifunctional MXene-coated cellulose yarns." *Adv. Funct. Mater.*, **29**, 1905015 (2019).
35. Y. Xie and P. R. C. Kent, "Hybrid density functional study of structural and electronic properties of functionalized $Ti_{n+1}X_n(X = C, N)$ monolayers.." *Physical Review B*, **87**, 235441 (2013).
36. C. Eames and M. S. Islam, "Ion intercalation into two-dimensional transition-metal carbides: global screening for new high-capacity battery materials." *J. Am. Chem. Soc.*, **136**, 16270 (2014).
37. Y. Xie, Y. Dall'Agnese, M. Naguib, Y. Gogotsi, M. W. Barsoum, H. L. Zhuang, and P. R. Kent, "Prediction and characterization of MXene nanosheet anodes for non-lithium-ion batteries." *ACS Nano*, **8**, 9606 (2014).
38. Y. Xie, M. Naguib, V. N. Mochalin, M. W. Barsoum, Y. Gogotsi, X. Yu, K. W. Nam, X. Q. Yang, A. I. Kolesnikov, and P. R. Kent, "Role of surface structure on Li-ion energy storage capacity of two-dimensional transition-metal carbides." *J. Am. Chem. Soc.*, **136**, 6385 (2014).
39. G. Deysher et al., "Synthesis of Mo_4VAlC_4 MAX phase and two-dimensional Mo_4VC_4 MXene with five atomic layers of transition metals.." *ACS Nano*, **14**, 204 (2020).
40. M. Alhabeb, K. Maleski, B. Anasori, P. Lelyukh, L. Clark, S. Sin, and Y. Gogotsi, "Guidelines for synthesis and processing of two-dimensional Titanium Carbide ($Ti_3C_2T_x$ MXene)." *Chem. Mater.*, **29**, 7633 (2017).
41. M. W. Barsoum and M. Radovic, "Elastic and mechanical properties of the MAX Phases." *Annu. Rev. Mater. Res.*, **41**, 195 (2011).
42. Y.-Y. Peng, B. Akuzum, N. Kurra, M.-Q. Zhao, M. Alhabeb, B. Anasori, E. C. Kumbur, H. N. Alshareef, M.-D. Ger, and Y. Gogotsi, "All-MXene (2D titanium carbide) solid-state micro-supercapacitors for on-chip energy storage." *Energy Environ. Sci.*, **9**, 2847 (2016).
43. L. Agartan, K. Hantanasirisakul, S. Buczek, B. Akuzum, K. A. Mahmoud, B. Anasori, Y. Gogotsi, and E. C. Kumbur, "Influence of operating conditions on the desalination performance of a symmetric pre-conditioned $Ti_3C_2T_x$ -MXene membrane capacitive deionization system." *Desalination*, **477**, 114267 (2020).
44. L. Wei, C. Xiong, H. R. Jiang, X. Z. Fan, and T. S. Zhao, "Highly catalytic hollow $Ti_3C_2T_x$ MXene spheres decorated graphite felt electrode for vanadium redox flow batteries." *Energy Storage Mater.*, **25**, 885 (2020).
45. C. E. Shuck and Y. Gogotsi, "Taking MXenes from the lab to commercial products." *Chem. Eng. J.*, **401**, 125786 (2020).
46. S. Uzun, M. Han, C. J. Strobel, K. Hantanasirisakul, A. Goad, G. Dion, and Y. Gogotsi, "Highly conductive and scalable $Ti_3C_2T_x$ -coated fabrics for efficient electromagnetic interference shielding." *Carbon*, **174**, 382 (2021).
47. S. Uzun, M. Schelling, K. Hantanasirisakul, T. S. Mathis, R. Askeland, G. Dion, and Y. Gogotsi, "Additive-free aqueous MXene inks for thermal inkjet printing on textiles." *Small*, **17**, 2006376 (2020).
48. K. Maleski, C. E. Ren, M.-Q. Zhao, B. Anasori, and Y. Gogotsi, "Size-dependent physical and electrochemical properties of two-dimensional MXene flakes." *ACS Appl. Mater. Interfaces*, **10**, 24491 (2018).
49. I. Ihsanullah, "Potential of MXenes in water desalination: current status and perspectives." *Nano-Micro Letters*, **12**, 72 (2020).
50. B. Akuzum, K. Maleski, B. Anasori, P. Lelyukh, N. J. Alvarez, E. C. Kumbur, and Y. Gogotsi, "Rheological characteristics of 2D Titanium Carbide (MXene) dispersions: a guide for processing MXenes." *ACS Nano*, **12**, 2685 (2018).
51. C. R. Dennison, E. Agar, B. Akuzum, and E. C. Kumbur, "Enhancing mass transport in redox flow batteries by tailoring flow field and electrode design." *J. Electrochem. Soc.*, **163**, A5163 (2015).
52. B. Akuzum, Y. C. Alparslan, N. C. Robinson, E. Agar, and E. C. Kumbur, "Obstructed flow field designs for improved performance in vanadium redox flow batteries." *J. Appl. Electrochem.*, **49**, 551 (2019).
53. I. Mayrhuber, C. R. Dennison, V. Kalra, and E. C. Kumbur, "Laser-perforated carbon paper electrodes for improved mass-transport in high power density vanadium redox flow batteries." *J. Power Sources*, **260**, 251 (2014).

54. A. J. Bard and L. R. Faulkner, *Electrochemical Methods: Fundamentals and Applications* (Wiley, New York, NY) (2000)978-0-471-04372-0.
55. J.-H. Kim, K. J. Kim, M.-S. Park, N. J. Lee, U. Hwang, H. Kim, and Y.-J. Kim, "Development of metal-based electrodes for non-aqueous redox flow batteries." *Electrochem. Commun.*, **13**, 997 (2011).
56. D. Aaron, Z. Tang, A. B. Papandrew, and T. A. Zawodzinski, "Polarization curve analysis of all-vanadium redox flow batteries." *J. Appl. Electrochem.*, **41**, 1175 (2011).
57. C.-N. Sun, F. M. Delnick, D. S. Aaron, A. B. Papandrew, M. M. Mench, and T. A. Zawodzinski, "Resolving losses at the negative electrode in all-vanadium redox flow batteries using electrochemical impedance spectroscopy." *J. Electrochem. Soc.*, **161**, A981 (2014).
58. M. Zhang, M. Moore, J. S. Watson, T. A. Zawodzinski, and R. M. Counce, "Capital cost sensitivity analysis of an all-vanadium redox-flow battery." *J. Electrochem. Soc.*, **159**, A1183 (2012).
59. A. M. Pezeshki, J. T. Clement, G. M. Veith, T. A. Zawodzinski, and M. M. Mench, "High-performance electrodes in vanadium redox flow batteries through oxygen-enriched thermal activation." *J. Power Sources*, **294**, 333 (2015).
60. H. Sun et al., "Vanadium redox flow batteries fabricated by 3D printing and employing recycled vanadium collected from ammonia slag." *J. Electrochem. Soc.*, **166**, B3125 (2019).
61. G. Qiu, C. R. Dennison, K. W. Knehr, E. C. Kumbur, and Y. Sun, "Pore-scale analysis of effects of electrode morphology and electrolyte flow conditions on performance of vanadium redox flow batteries." *J. Power Sources*, **219**, 223 (2012).
62. B. Sun and M. Skyllas-Kazacos, "Chemical modification of graphite electrode materials for vanadium redox flow battery application-part II. Acid treatments." *Electrochimica Acta* , **37**2459 (1992).
63. H. Ishitobi, S. Sugawara, K. Oba, T. Hirano, H. Doki, Y. Handa, Y. Sato, S. Yamamoto, and N. Nakagawa, "Highly Active Electrode With Efficiently Added Surface Oxygen Groups for a Vanadium Redox Flow Battery." *Journal of Electrochemical Energy Conversion and Storage*, **17**031001 (2019).
64. J. Maruyama, T. Hasegawa, S. Iwasaki, T. Fukuhara, and M. Nogami, "Mechanism of dioxovanadium ion reduction on oxygen-enriched carbon surface." *J. Electrochem. Soc.*, **160**, A1293 (2013).
65. Y. Li, J. Parrondo, S. Sankarasubramanian, and V. Ramani, "Impact of surface carbonyl- and hydroxyl-group concentrations on electrode kinetics in an all-vanadium redox flow battery." *The Journal of Physical Chemistry C*, **123**, 6370 (2019).
66. M. Park, I.-Y. Jeon, J. Ryu, H. Jang, J.-B. Back, and J. Cho, "Edge-halogenated graphene nanoplatelets with F, Cl, or Br as electrocatalysts for all-vanadium redox flow batteries." *Nano Energy*, **26**, 233 (2016).
67. M. Park, I.-Y. Jeon, J. Ryu, J.-B. Baek, and J. Cho, "Exploration of the effective location of surface oxygen defects in graphene-based electrocatalysts for all-vanadium redox-flow batteries." *Adv. Energy Mater.*, **5**, 1401550 (2015).